Nano-infrared imaging and spectroscopy of hot-electron plasmons in graphene

Yilong Luan[1,2], Marek Kolmer[2], Michael C. Tringides[1,2], Zhe Fei[1,2]*

[1]Department of Physics and Astronomy, Iowa State University, Ames, Iowa 50011, USA
[2]Ames Laboratory, U.S. Department of Energy, Iowa State University, Ames, Iowa 50011, USA

*Correspondence to: (Z.F.) zfei@iastate.edu

ABSTRACT

We report a nano-infrared (IR) imaging and spectroscopy study of hot-electron plasmons in graphene, which are excited by the sharp metallic probe of the scattering-type scanning near-field optical microscope (s-SNOM) illuminated with a mid-IR femtosecond (fs) pulsed laser. We found the average electron temperature (T_e) can reach as high as ~1400 K within the pulse duration, which can be controlled by tuning the laser power. With s-SNOM, we monitored both the plasmon interference fringes and the hybrid plasmon-phonon resonances of graphene. When graphene is heavily doped, a higher T_e leads to a smaller plasmon wavelength and a weaker plasmon-phonon resonance intensity. At the charge neutrality point, on the other hand, the plasmon-phonon resonance intensity is enhanced when T_e increases. With quantitative modeling and theoretical analysis, we concluded that the observed plasmonic responses of hot electrons are governed by the temperature dependencies of chemical potential, electron scattering, and thermal carrier generation. The competition of these factors leads to distinct T_e-dependence of graphene plasmons at various doping levels.

I. INTRODUCTION

Graphene is a prototypical two-dimensional (2D) material formed by a sheet of carbon atoms in a honeycomb lattice. The unique lattice structure has symmetry properties that lead to a cone-shaped Dirac dispersion close to the charge neutrality point, so low-energy electronic excitations behave as massless Dirac Fermions. Surface plasmons of graphene are generated due to the collective oscillations of these Dirac fermions spanning a wide spectral region from terahertz to infrared (IR) [1-3]. They have demonstrated many superior properties such as gate tunability, long propagation length, and high spatial confinement [4-17], which leads to many promising optoelectronic and nanophotonic applications [18-23]. Besides the potential applications, the fundamental properties associated with graphene plasmons also attract a lot of research interest. For example, a recent study of graphene plasmons at cryogenic temperatures uncovers the fundamental limits of the plasmonic parameters in graphene [16]. At the high-temperature regime, graphene plasmons due to hot carriers generated by ultrafast optical pumping have also been studied [24,25]. Nevertheless, these pump-probe studies were performed in graphene at fixed doping levels. A comprehensive study of graphene at various carrier densities is needed to get a more complete picture of hot-electron plasmons.

Here we report a systematical nano-IR imaging and spectroscopy study of the plasmonic responses of hot electrons in graphene. Our graphene samples were fabricated by mechanical exfoliations of bulk graphite onto the standard SiO_2/Si substrates that facilitate back gating. To generate and characterize hot-electron plasmons, we employed a scattering-type scanning near-field optical microscope (s-SNOM) that is excited by a broadband mid-IR femtosecond (fs) laser [Fig. 1(a)]. The mid-IR pulses have a pulse width of about 100 fs and a repetition rate of 80 MHz. The average laser power is up to 250 μW at the spectral range of 700 - 1200 cm^{-1} which is suitable for the studies of graphene plasmons [Fig. 1(b)]. The sharp and metallic s-SNOM tip not only bridges the momentum mismatch from photons to plasmons but also strongly enhances the excitation laser field. Due to the tip enhancement, the peak field strength underneath the tip surpasses 100 kV/cm, so electrons can be heated up to very high temperatures [24]. With an IR attenuator, we can control the laser power and hence the average electron temperature in graphene. Additional information about the experimental setup is given in Appendix A.

II. RESULTS AND DISCUSSIONS

A. Broadband nano-IR imaging of hot-electron plasmons

With s-SNOM excited with the fs pulsed laser, we performed nano-IR imaging and spectroscopy of hot-electron plasmons. The experimental observable of s-SNOM discussed here is the near-field scattering amplitude (s). In Fig. 1(c,d), we plot two hyperspectral images of graphene $s(x, \omega)$ taken at two different laser powers (P), where the horizontal and vertical axes correspond to tip location (x) and IR frequency (ω), respectively. Each hyperspectral map consists of a few tens of nano-IR spectra taken as tip scans step by step (step size = 25 nm) perpendicular to the edge of graphene. Here the graphene sample is highly hole-doped with a carrier density of about 7.2×10^{12} cm^{-2}, corresponding to a gate voltage of V_g-V_{CN} = -100 V, where V_{CN} is the charge-neutrality voltage pre-determined by s-SNOM imaging with a continuous-wave (CW) laser (see Appendix C). The spectral window of the hyperspectral maps shown in Fig. 1(c,d) is 850-1150 cm^{-1}. As shown in the calculated dispersion diagram (see Appendix D for the calculate method) of the graphene/SiO_2 interface [Fig. 1(b)], the spectral window (marked with an arrow) is sandwiched between the two optical phonons of SiO_2 (marked with white dashed lines), so the nano-IR response of graphene within the spectral range is mainly due to surface plasmons of graphene.

In the hyperspectral map taken with a lower laser power [P = 20 μW, Fig. 1(b)], the dominant feature is the bright fringe (marked with a black dashed curve) close to the sample edge at $x = 0$ nm (marked with a white dashed line), which shows a clear dependence on IR frequency. More specifically, the bright fringe becomes broader and slightly further away from the sample edge at lower IR frequencies. According to previous studies [12,13], the bright fringe is formed due to the constructive interference between tip-launched plasmons and those reflected from the sample edge. As a result, both the fringe width (or period) and the fringe-edge distance are proportional to the plasmon wavelength $\lambda_p \equiv 2\pi/\mathrm{Re}(q_p)$, where q_p is the complex plasmon wavevector. Due to the dispersion nature of graphene plasmons, q_p and λ_p are sensitively dependent on IR frequency as shown in the calculated dispersion diagram of graphene plasmons [Fig. 1(b)], so the bright fringe is expected to evolve with frequency as observed in Fig. 1(c). As the average laser power increases to 250 μW [Fig. 1(d)], the fringe becomes much weaker and narrower compared to that shown in the low-power image [Fig. 1(c)].

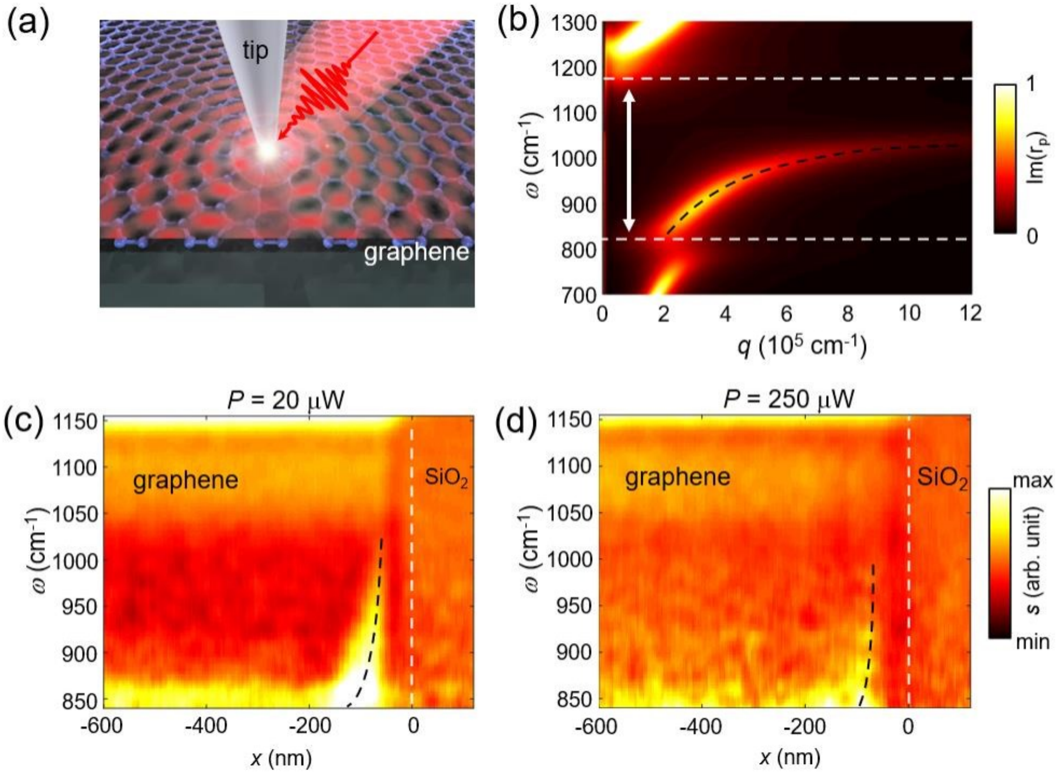

FIG. 1. (a) Illustration of the s-SNOM experiment of graphene excited by an fs pulsed laser. (b) Calculated dispersion diagram of plasmons at the graphene/SiO_2 interface. The white dashed lines marked the two optical phonons of SiO_2. The black dashed curve marks the segment of graphene plasmons that we were measuring. (c,d), The hyperspectral images of graphene close to its edge taken with the laser powers of P = 20 μW and 250 μW, respectively.

B. Numerical modeling of the plasmon fringe profiles

For quantitative analysis, we took horizontal line profiles from Fig. 1(c,d) at various frequencies away from the two SiO_2 phonons. A selected set of profiles are plotted in Fig. 2 as grey curves, where the peaks shown correspond to the fringes in the hyperspectral maps. To fit the profiles, we adopted a quantitative s-SNOM model from previous literature [12]. In this model, the tip is approximated as a conducting spheroid, and the s-SNOM signals are obtained by evaluating the total radiating dipole moment of the tip. Note that we considered the standard signal modulation and demodulation processes of s-SNOM when computing the s-SNOM signals. Additional information about the s-SNOM model is given in Appendix B. The modeling parameter for graphene is the complex plasmon wavevector q_p, based on which we have the plasmon wavelength $\lambda_p \equiv 2\pi/\ \mathrm{Re}(q_p)$ and the plasmon damping rate $\gamma_p \equiv \mathrm{Im}(q_p)/\mathrm{Re}(q_p)$. The modeled fringe profiles are plotted in Fig. 2 as red curves, which match the experimental profiles (gray curves). From the modeling, we were able to extract both λ_p and γ_p of the graphene sample, which are proportional to the Drude weight and electron scattering rate of graphene, respectively.

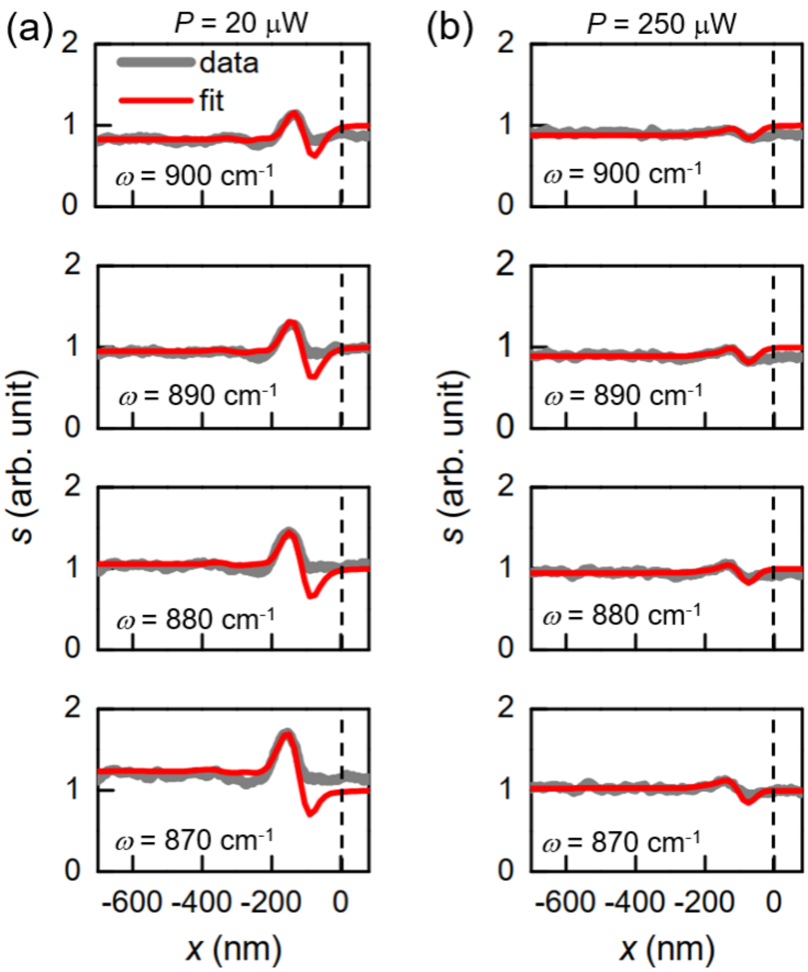

FIG. 2. Experimental (grey) and modeled (red) fringe profiles at various frequencies taken with $P = 20$ μW (a) and $P = 250$ μW (b), respectively. The experimental profiles were horizontal line cuts taken directly from the hyperspectral images in Fig. 1(c,d). The vertical dashed lines mark the edge of graphene.

The extracted λ_p and γ_p at various frequencies are plotted in Fig. 3(a,b) as data points. Here one can see that λ_p taken at $P = 250$ μW is smaller than that taken at $P = 20$ μW, and γ_p at $P = 250$ μW is significantly larger than that at $P = 20$ μW. Such an observation can be understood as electron heating effects when excited by tip-enhanced fs laser pulses. At higher electron temperatures, electrons will scatter more frequently with phonons, and impurities, so it is expected that plasmons will have higher damping. The temperature dependence of λ_p is due to the combined effects of chemical potential and thermal excited carriers, which will be discussed in detail below. Note that the electron heating due to fs pulses is a non-equilibrium process [24-27]. Electrons become thermalized shortly after the fs pulses arrive at the sample. They then gradually cool down due to the scattering of electrons with intrinsic phonons of graphene. Heat transfer from graphene to the SiO_2 substrate is a much slower process, typically in the order of tens to hundreds of picoseconds [28]. In the theoretical discussions below, we used a single effective temperature (T_e), which can be considered as the average temperature of electrons of graphene within the 100-fs pulse duration.

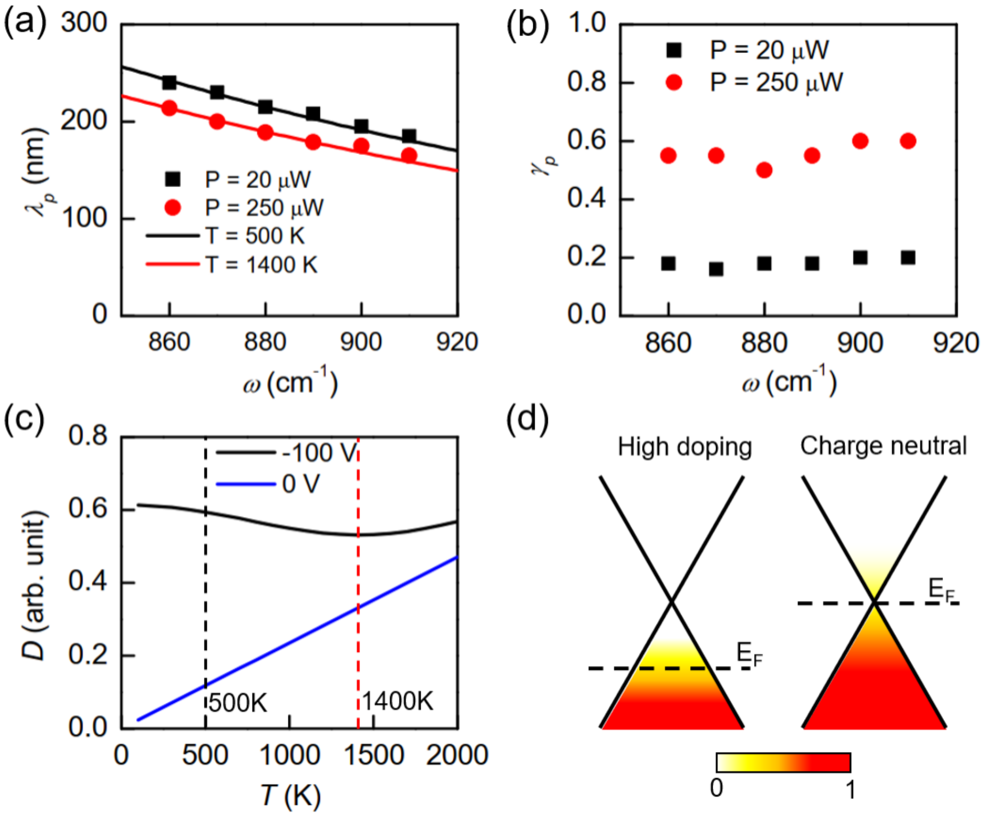

FIG. 3. (a) Frequency-dependent plasmon wavelength from both experiments ($P = 20$ μW and $P = 250$ μW) and calculations (T =500 K and T = 1500 K). (b) Frequency-dependent plasmon damping rates from experiments ($P = 20$ μW and $P = 250$ μW). (c) Calculate Drude weight versus electron temperature at V_g - V_{CN} = -100 V and 0 V. (d) Illustration of electron occupation close to the Fermi level for both doped and charge-neutral graphene at elevated temperatures.

C. Theoretical calculations of hot-electron plasmons

To understand theoretically the T_e-dependent plasmonic responses, we first write down the following relationship of q_p with the optical conductivity of graphene (σ):

$$q_p \approx \frac{i\varepsilon_0(1+\varepsilon_s)\omega}{\hbar\sigma}, \tag{1}$$

Here, $\hbar$ is the reduced plank constant, ε_0 is the vacuum permittivity, ε_s is the relative permittivity of the substrate, and σ is sensitively dependent on E and T_e.

The optical conductivity of graphene consists of both the interband (σ_{inter}) and intraband (σ_{intra}) components, which are both considered in our calculations. The interband part plays a less important role when graphene is highly doped due to Pauli blocking (see Appendix E for the equations of σ_{inter}). The intraband part is more responsible for overall plasmonic responses of graphene. Under Drude approximation, $\sigma_{\mathrm{intra}}(E)$ can be written as

$$\sigma_{\mathrm{intra}}(E) = \frac{i}{\pi\hbar}\frac{D}{\omega+i\gamma}, \tag{2}$$

where D and γ are the Drude weight and the charge scattering rate of graphene, respectively. With Eq. (1) and (2), we know that $\lambda_p \equiv 2\pi/\,\mathrm{Re}(q_p)$ is roughly proportional to D in doped graphene. The Drude weight is written as

$$D = \frac{8\sigma_0 k_B T_e}{\hbar} \ln\left\{2\cosh\left[\frac{\mu(T_e)}{2k_B T_e}\right]\right\}, \tag{3}$$

where $\sigma_0 = e^2/4\hbar$ is the universal conductivity, and $\mu(T_e)$ is the chemical potential and can be solved through the following equation.

$$-\mathrm{Li}_2(-e^{\mu/k_B T_e}) + -\mathrm{Li}_2(-e^{-\mu/k_B T_e}) = \frac{E_F^2}{2(k_B T)^2}, \tag{4}$$

where $\mathrm{Li}_2(x)$ is the dilogarithm function.

With Eqs. (1)-(3), we can obtain the T_e-dependence of D, which is plotted in Fig. 3(c) for graphene with various doping levels. For $V_g - V_{CN}$ = -100 V, D decreases systematically with increasing T_e over a broad temperature range below 1500 K. This is mainly due to the drop of chemical potential μ at higher T_e (see Appendix F). With the calculated D, we can obtain λ_p at various frequencies, gate voltages, and electron temperatures. By fitting experimental data in Fig. 3(a), we were able to estimate T_e of graphene to be about 500 ± 100 K for P = 20 μW and 1400 ± 200 K for P = 250 μW.

D. Nano-IR spectroscopy of the hybrid plasmon-phonon resonance

In Fig. 3(c), we also plot the calculated D for charge-neutral graphene, which increases linearly with T_e. The rapid increase of D with T_e is primarily due to the thermally-excited carriers as illustrated in the right panel of Fig. 3(d). Plasmons formed due to the collective excitations of pure thermal carriers in charge-neutral graphene are termed “intrinsic plasmons” of graphene [29]. These plasmons are typically very weak and strongly damped, so it is challenging to study them with the plasmon fringe imaging method used in Fig. 1(c,d). Instead, we performed nano-IR spectroscopy on the hybrid plasmon-phonon mode of graphene, which is formed due to the coupling between graphene plasmons and SiO_2 phonons [see Fig. 1(b)] [8]. Previous nano-IR studies of the hybrid plasmon-phonon mode are mainly focused on highly-doped graphene samples [8,24]. Here we explore hybrid plasmon-phonon mode at all doping levels (including the charge-neutrality point) and different laser powers. Note that the signal of the hybrid resonance peak is higher than that of gold and is at least two orders of magnitude higher than that of the noise background. Therefore, it is very convenient to monitor small changes of plasmonic parameters of graphene by measuring the hybrid plasmon-phonon resonance mode.

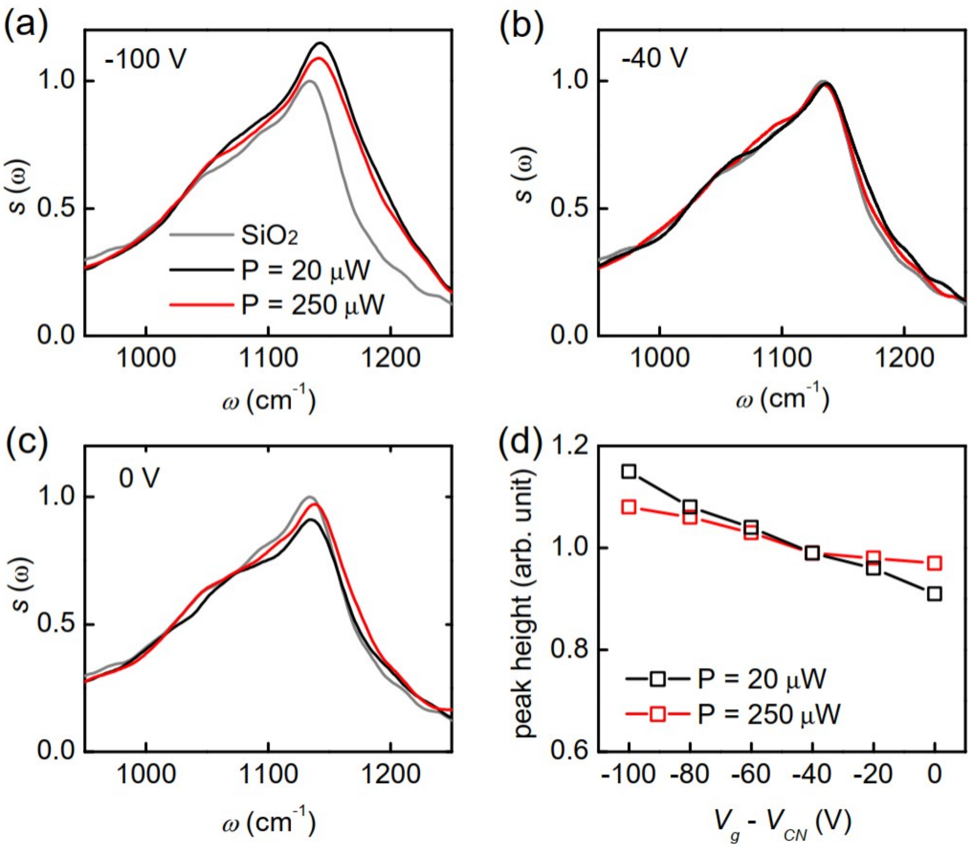

FIG. 4. (a-c) The nano-IR spectra of SiO_2 (grey) and graphene with three gate voltages (V_g-V_{CN}) taken at two laser powers: $P = 250$ μW (black) and 20 μW (red). (d) The peak height of the hybrid plasmon-phonon resonance versus V_g-V_{CN}.

In Fig. 4(a), we plot a selected dataset of plasmon-phonon resonance spectra of graphene at gate-controlled doping levels: high doping ($V_g - V_{CN}$ = -100 V), intermediate doping ($V_g - V_{CN}$ = -40 V), and charge-neutrality point ($V_g - V_{CN} \approx 0$ V), each measured with two laser powers: $P = 20$ μW (black curve) and $P = 250$ μW (red curve). All these spectra were taken in the interior of graphene to avoid the plasmon interference fringes at the sample edges (see Fig. 1). The spectrum of the bare SiO_2/Si substrate (grey curve) is also shown in Fig. 4 as a reference. The dominant feature of the spectrum of the bare SiO_2 substrate is the strong IR phonon resonance at around 1130 cm^{-1}. After adding the highly-doped graphene ($V_g - V_{CN}$ = -100 V) on top of SiO_2, the IR resonance is enhanced and higher than that of the bare SiO_2 phonon [Fig. 4(a)] – the signature behavior of the hybrid plasmon-phonon mode formed by plasmon-phonon coupling [8]. Moreover, the resonance peak appears to be weaker at higher laser power ($P = 250$ μW) and stronger at lower power ($P = 20$ μW). This is due to the drop of Drude weight D and the increase of plasmon damping rate γ_p at the higher laser power, which is consistent with the plasmon fringe data (Figs. 1 and 2). For the intermediate-doped graphene ($V_g - V_{CN}$ = -40 V), the resonance enhancement is not clearly seen, and the peak height of the hybrid plasmon-phonon resonance of graphene is closer to that of the phonon resonance of SiO_2 [Fig. 4(a)]. Besides, there is no clear difference in resonance height measured with two laser powers. In the case of charge-neutrality point ($V_g - V_{CN}$ = 0 V) [Fig. 4(c)], the peak height of the hybrid plasmon-phonon resonance of graphene is lower than that of the bare phonon resonance of SiO_2. More interestingly, the resonance peak taken with $P = 250$ μW (red curve) is higher than that taken with $P = 20$ μW (blue curve), which is contrary to the high-doping case [Fig. 4(a)]. We attribute the higher resonance peak at $P = 250$ μW to thermally-excited carriers [Fig. 3(d)], which significantly increases the Drude weight D of graphene [Fig. 3(c)].

The spectroscopic behaviors discussed above are summarized in Fig. 4(d), where we plot the resonance peak height versus gate voltages taken with two laser powers (P = 20 μW and P = 250 μW). From Fig. 4(d), one can see a clear trend of decrease of resonance height at lower $|V_g - V_{CN}|$ for both laser powers. This is mainly due to the drop of Drude weight at lower doping, resulting in a weaker plasmon-phonon coupling and hence less phonon enhancement [8]. Another factor is related to the plasmon damping that originates partially from the electron-impurity scattering. Scattering of electrons with impurities becomes stronger at lower doping levels due to the reduction of screening of impurities by free charges. As a result, plasmon damping increases and the plasmon-phonon resonances weakens. Comparing the two curves, the low-power one drops faster than the other one at smaller $|V_g - V_{CN}|$ resulting in a clear crossover at intermediate voltages. As discussed above, the crossover is a signature of competition of multiple thermal effects including thermal excitation of carriers, negative temperature dependence of chemical potential (see Appendix F), and enhanced electron scatterings at high temperatures.

III. CONCLUSION

We have performed a comprehensive study of the plasmonic responses of hot electrons in graphene by using the s-SNOM excited with a mid-IR pulsed laser. We found that the fs laser pulses with further enhancement by the s-SNOM tip can significantly heat up graphene electrons, leading to unique plasmonic responses in both the plasmon interference fringes and the hybrid plasmon-phonon resonance. With quantitative modeling and analysis, we concluded that the hot-electron plasmonic responses can be understood by three major factors, namely the drop of chemical potential, the increase of electron scattering rate, and the excitation of thermal carriers at higher T_e. Moreover, we were able to control the competition of these factors by tuning the carrier density and electron temperature of graphene. Our work deepens the understanding of graphene plasmons at elevated electron temperatures and paves the way for future studies of hot-electron plasmonic responses of other novel materials.

ACKNOWLEDGMENTS

Work done at Ames Lab was supported by the U.S. Department of Energy, Office of Basic Energy Science, Division of Materials Sciences and Engineering. Ames Laboratory is operated for the U.S. Department of Energy by Iowa State University under Contract No. DE-AC02-07CH11358. The sample fabrication and characterization were supported by the National Science Foundation under Grant No. DMR-1945560.

APPENDIX A: EXPERIMENTAL SETUP

The nano-optical imaging and spectroscopy measurements were performed using a scattering-type scanning near-field optical microscope (s-SNOM) from Neaspec GmbH, which was built on a tapping-mode atomic force microscope (AFM). The AFM tips used in our measurements are Pt/Ir coated silicon tips (Arrow NCPT tips from NanoAndMore). The tapping frequency of the tips is close to 270 kHz and the tapping amplitude is close to 100 nm. For continuous-wave (CW) laser imaging (see Appendix C), we excited the s-SNOM with a continuous-wave CO_2 laser (Access Laser) with a laser frequency set to be ω = 883 cm^{-1}. For broadband imaging and spectroscopy, we excited the s-SNOM with a broadband fs laser from Toptica Photonics. These fs laser pulses are generated in a GaSe crystal by different-frequency mixing of near-IR pulses from an Er-doped fiber laser and synchronized supercontinuum pulses, and they have a pulse width of about 100 fs and a repetition rate of 80 MHz. The spectral window chosen for the measurements is from 700-1200 cm^{-1}. The maximum laser power in this window is about 250 μW and we can reduce the laser power to 20 μW with an IR attenuator. As discussed in the main text, the key advantage of fs-laser illuminated s-SNOM is the capability to study hot-electron responses of the sample due to the high peak field strength. If adding an additional fs pump laser [24,25], one can study the ultrafast dynamics and transient responses of the system. To study normal responses of the electronic system without extremely high electron temperatures, a laser attenuator or pulse elongator [24] is needed.

APPENDIX B: QUANTITATIVE s-SNOM MODEL

To extract the plasmonic parameters of graphene, we adopted the numerical model from previous work [12]. In this model, we compute quantitatively the s-SNOM signals of graphene that supports propagative plasmons. The s-SNOM tip is modeled as an elongated conducting spheroid, which is a common approach in s-SNOM modeling. The radius of curvature at the two ends of the spheroid was set to be ~25 nm, which is consistent with our tip parameter. The length of the spheroid was set to be 25 times the tip radius. The s-SNOM signal is approximately proportional to the electrical field (E_z) underneath the tip as well as the total dipole moment (p_z) of the tip. Graphene is modeled as a plasmonic medium with a complex plasmon wavevector $q_p = q_1 + iq_2$. The plasmon wavelength is $\lambda_p \equiv 2\pi/q_1$, and the plasmon damping rate is $\gamma_p \equiv q_2/q_1$. In addition, we also considered signal modulation and demodulation due to the tip tapping in the modeling.

APPENDIX C: PLASMON IMAGING WITH A CW LASER

In addition to the broadband nano-imaging with the fs pulsed laser as discussed in the main text, we have also performed nano-IR imaging measurements of the same graphene sample with a continuous-wave (CW) IR laser. Here the laser frequency is set to be $\omega \approx 883$ cm^{-1}. By tuning the back-gate voltage, we were able to control the carrier density of graphene. The near-field amplitude images and the corresponding fringe profiles taken perpendicular to the sample edge are plotted in Fig. 5(a,b), respectively. Here, we observe 2-3 plasmon fringes when graphene is highly doped. As the carrier density decreases [from top to bottom panels in Fig. 5(a,b)] both the fringe width (or period) and the number of fringes decrease. At the charge neutrality point (V_g - V_{CN} = 0), no plasmon fringe can be seen. By fitting all the fringe profiles [Fig. 5(b)], we were able to determine λ_p and γ_p of graphene at different gate voltages [Fig. 5(c,d)]. As shown in Fig. 5(c), the experimental λ_p (data points) increases systematically with doping. The measured γ_p with CW laser is in the range from 0.12 to 0.18 [Fig. 5(d)] with slightly lower γ_p at high doping regime. Overall, the gating results shown in Fig. 5 taken with a CW laser are consistent with previous studies [12,13], confirming the overall good quality and functionality of our graphene devices.

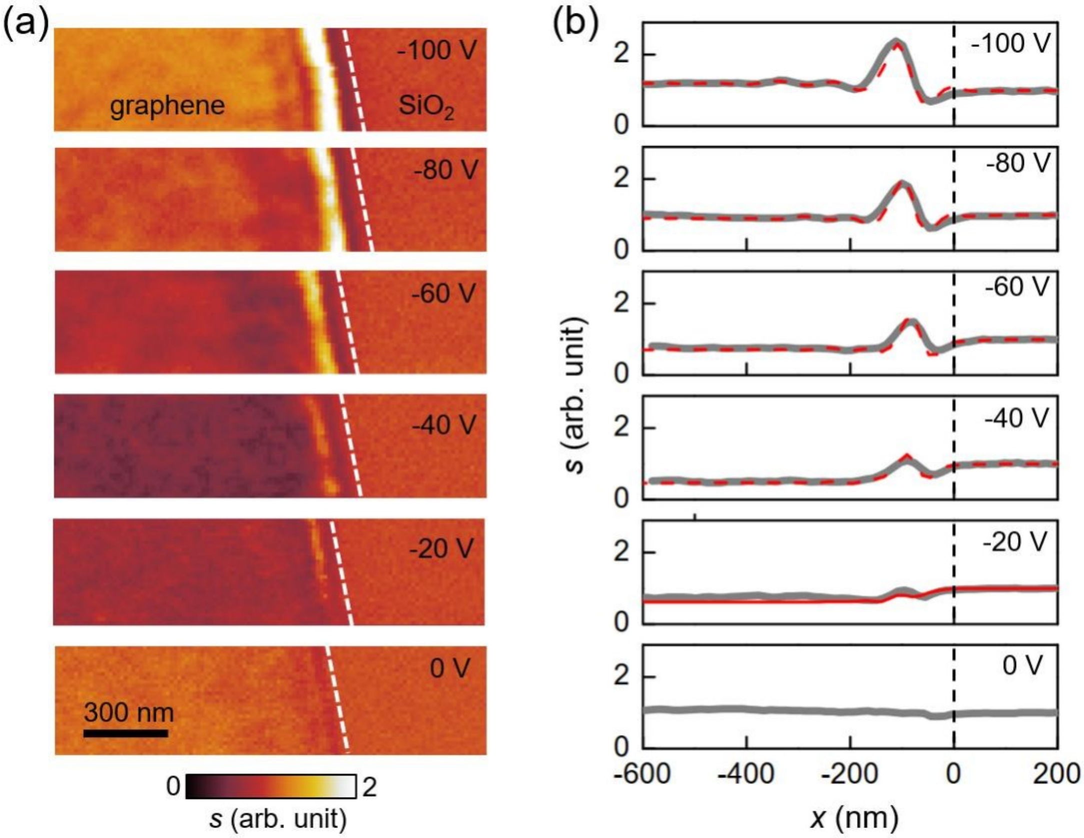

FIG. 5. (a) Nano-IR imaging data taken with a CW laser at ω = 883 cm^{-1} at various gate voltages (V_g - V_{CN}). The white dashed lines mark the sample edge. (b) Plasmon fringe profiles taken perpendicular to the images in (a). The edge of graphene is at x = 0.

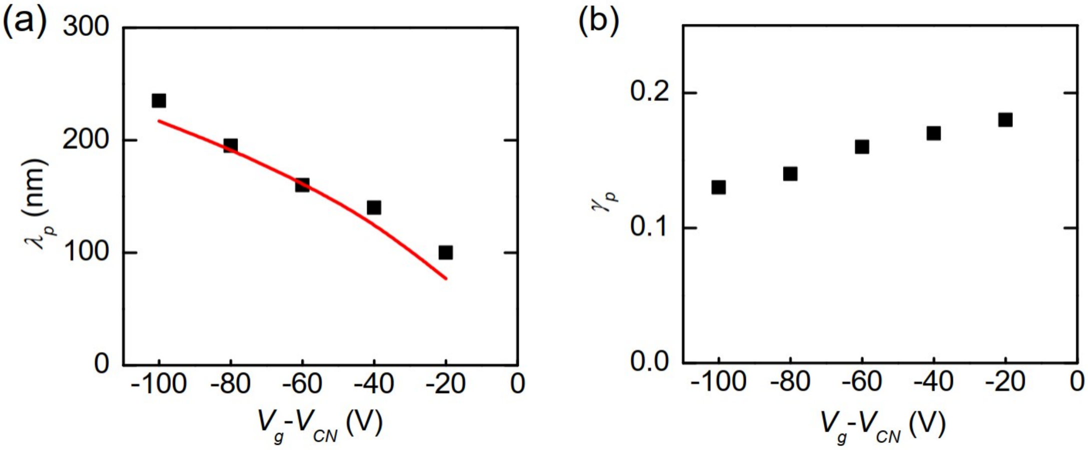

FIG. 6. The extracted plasmon wavelength λ_p and damping rate γ_p versus V_g - V_{CN}. The red curve in (a) is the theoretical calculation with Eqs. 1-3 of graphene plasmons at room temperature.

APPENDIX D: DISPERSION CALCULATIONS

In Fig. 1(b) of the main text, we plot the dispersion diagrams of graphene plasmons. Here the colormap corresponds to the imaginary part of the p-polarization reflection coefficient Im(r_p). To calculate Im(r_p), we used the transfer matrix method and considered the entire graphene/SiO$_2$/Si multilayer structure. The optical conductivity of graphene is calculated with Eq. 1-4. The bright curves shown in the dispersion colormaps in Fig. 1(b) correspond to the plasmon mode that shows coupling with the two optical phonons of SiO_2 [8]. The dispersion calculation method has been widely applied in the studies of plasmons and polaritons in other materials.

APPENDIX E: INTERBAND COMPONENT OF OPTICAL CONDUCTIVITY

In our modeling of graphene, we consider both the intraband and interband components of optical conductivity. The intraband component is introduced in the main text. Here we show the equation of the interband component $\sigma_{\text{inter}}(E,T_e)$, which is responsible for the Landau damping of plasmons:

$$\sigma_{\text{inter}} = \sigma_0 H\left(\frac{E}{2}\right) + \frac{4iE}{\pi}\sigma_0 \int_0^\infty dx \frac{H(x) - H(E/2)}{E^2 - 4x^2}, \tag{5}$$

where

$$H(x) = \frac{\sinh(x/k_B T_e)}{\cosh(E_F/k_B T_e) + \cosh(x/k_B T_e)}. \tag{6}$$

APPENDIX F: TEMPERATURE DEPENDENCE OF CHEMICAL POTENTIAL

In Fig. 7, we show a plot of the temperature dependence curves of chemical potential μ at various gate voltages (V_g-V_{CN}). One can see from Fig. 7 that μ decreases systematically with increasing T. Such a temperature dependence of μ is an expected thermodynamic behavior because $\partial\mu/\partial T_e \approx -S$, where S is the entropy of the system. As discussed in the main text, the T-dependence of μ is mainly responsible for the decrease of D and λ_p as T_e increases in highly-doped graphene.

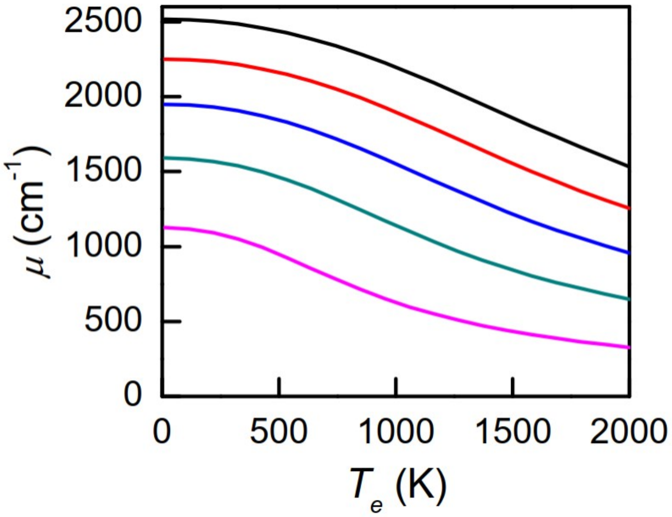

FIG. 7. Temperature-dependence of the chemical potential of graphene at various gate voltages (V_g-V_{CN}).

References

[1] V. Ryzhii, A. Satou, and T. Otsuji, Plasma waves in two-dimensional electron-hole system in gated graphene heterostructures, J. Appl. Phys. **101**, 024509 (2007).

[2] M. Jablan, H. Buljan, and M. Soljačić, Plasmonics in graphene at infrared frequencies, Phys. Rev. B **80**, 245435 (2009).

[3] F. H. L. Koppens, D. E. Chang, and F. Javier García de Abajo, Graphene Plasmonics: A Platform for Strong Light–Matter Interactions, Nano Lett. **11**, 3370-3377 (2011).

[4] A. N. Grigorenko, M. Polini, and K. S. Novoselov, Graphene plasmonics, Nat. Photon. **6**, 749-758 (2012).

[5] D. N. Basov, M. M. Fogler, and F. J. García de Abajo, Polaritons in van der Waals materials, Science **354**, 195-195 (2016).

[6] T. Low, A. Chaves, J. D. Caldwell, A. Kumar, N. X. Fang, P. Avouris, T. F. Heinz, F. Guinea, L. Martin-Moreno, and F. Koppens, Polaritons in layered two-dimensional materials, Nat. Mater. **16**, 182–194 (2017).

[7] L. Ju, B. Geng, J. Horng, C. Girit, M. Martin, Z. Hao, H. A. Bechtel, X. Liang, A. Zettl, Y. R. Shen, F. Wang, Graphene plasmonics for tunable terahertz metamaterials, Nat. Nanotechnol. **6**, 630-634 (2011).

[8] Z. Fei, G. O. Andreev, W. Bao, L. M. Zhang, A. S. McLeod, C. Wang, M. K. Stewart, Z. Zhao, G. Dominguez, M. Thiemens, M. M. Fogler, M. J. Tauber, A. H. Castro-Neto, C. N. Lau, F. Keilmann, and D. N. Basov, Infrared Nanoscopy of Dirac Plasmons at the Graphene–SiO_2 Interface, Nano Lett. **11**, 4701-4705 (2011).

[9] V. W. Brar, M. S. Jang, M. Sherrott, J. J. Lopez, H. Atwater, Highly Confined Tunable Mid-Infrared Plasmonics in Graphene Nanoresonators, Nano Lett. **13**, 2541-2547 (2013).

[10] Z. Fang, S. Thongrattanasiri, A. Schlather, Z. Liu, L. Ma, Y. Wang, P. Ajayan, P. Nordlander, N. J. Halas, and F. J. G. de Abajo, Gated Tunability and Hybridization of Localized Plasmons in Nanostructured Graphene, ACS Nano **7**, 2388-2395 (2013).

[11] W. Gao, G. Shi, Z. Jin, J. Shu, Q. Zhang, R. Vajtai, P. M. Ajayan, J. Kono, and Q. Xu, Excitation and Active Control of Propagating Surface Plasmon Polaritons in Graphene, Nano Lett. **13**, 3698-3702 (2013).

[12] Z. Fei, A. S. Rodin, G. O. Andreev, W. Bao, A. S. McLeod, M. Wagner, L. M. Zhang, Z. Zhao, M. Thiemens, G. Dominguez, M. M. Fogler, A. H. Castro Neto, C. N. Lau, F. Keilmann, and D. N. Basov, Gate-tuning of graphene plasmons revealed by infrared nano-imaging, Nature **487**, 82-85 (2012).

[13] J. Chen, M. Badioli, P. Alonso-González, S. Thongrattanasiri, F. Huth, J. Osmond, M. Spasenović, A. Centeno, A. Pesquera, P. Godignon, A. Z. Elorza, N. Camara, F. J. García de Abajo, R. Hillenbrand, and F. H. L. Koppens, Optical nano-imaging of gate-tunable graphene plasmons, Nature **487**, 77-81 (2012).

[14] H. Yan, T. Low, W. Zhu, Y. Wu, M. Freitag, X. Li, F. Guinea, P. Avouris, and F. Xia, Damping pathways of mid-infrared plasmons in graphene nanostructures, Nat. Photon. **7**, 394-399 (2013).

[15] A. Woessner, M. B. Lundeberg, Y. Gao, A. Principi, P. Alonso-González, M. Carrega, K. Watanabe, T. Taniguchi, G. Vignale, M. Polini, J. Hone, R. Hillenbrand, and F. H. L. Koppens, Highly confined low-loss plasmons in graphene–boron nitride heterostructures, Nat. Mater. **14**, 421-425 (2015).

[16] G. X. Ni, A. S. McLeod, Z. Sun, L. Wang, L. Xiong, K. W. Post, S. S. Sunku, B.-Y. Jiang, J. Hone, C. R. Dean, M. M. Fogler, and D. N. Basov, Fundamental limits to graphene plasmonics, Nature **557**, 530-533 (2018).

[17] H. Hu, R. Yu, H. Teng, D. Hu, N. Chen, Y. Qu, X. Yang, X. Chen, A. S. McLeod, P. Alonso-González, X. Guo, C. Li, Z. Yao, Z. Li, J. Chen, Z. Sun, M. Liu, F. Javier García de Abajo, Q. Dai, Active control of micrometer plasmon propagation in suspended graphene, Nat. Commun. 13, 1465 (2022).

[18] T. Low and P. Avouris, Graphene Plasmonics for Terahertz to Mid-Infrared Applications, ACS Nano **8**, 1086 (2014).

[19] Q. Bao and K. P. Loh, Graphene Photonics, Plasmonics, and Broadband Optoelectronic Devices, ACS Nano **6**, 3677-3694 (2012).

[20] H. Hu, X. Yang, X. Guo, K. Khaliji, S. R. Biswas, F. Javier García de Abajo, T. Low, Z. Sun, and Q. Dai., Gas identification with graphene plasmons, Nat. Commun. **10**, 1131 (2019).

[21] N. Jr. Bareza, K. K. Gopalan, R. Alani, B. Paulillo, and V. Pruneri, Mid-infrared Gas Sensing Using Graphene Plasmons Tuned by Reversible Chemical Doping, ACS Photonics **7**, 4, 879–884 (2020).

[22] Y. Li, H. Yan, D. B. Farmer, X. Meng, W. Zhu, R. M. Osgood, T. F. Heinz, and P. Avouris, Graphene Plasmon Enhanced Vibrational Sensing of Surface-Adsorbed Layers, Nano Lett. **14**, 3, 1573–1577 (2014).

[23] D. B. Farmer, P. Avouris, Y. Li, T. F. Heinz, and S.-J. Han, Ultrasensitive Plasmonic Detection of Molecules with Graphene, ACS Photonics **3**, 4, 553–557 (2016).

[24] M. Wagner, Z. Fei, A. S. McLeod, A. S. Rodin, W. Bao, E. G. Iwinski, Z. Zhao, M. Goldflam, M. Liu, G. Dominguez, M. Thiemens, M. M. Fogler, A. H. Castro Neto, C. N. Lau, S. Amarie, F. Keilmann, D. N. Basov, Ultrafast and nanoscale plasmonic phenomena in exfoliated graphene revealed by infrared pump–probe nanoscopy, Nano Lett. **14**, 894-900 (2014).

[25] G. X. Ni, L. Wang, M. D. Goldflam, M. Wagner, Z. Fei, A. S. McLeod, M. K. Liu, F. Keilmann, B. Özyilmaz, A. H. Castro Neto, J. Hone, M. M. Fogler, D. N. Basov, Ultrafast optical switching of infrared plasmon polaritons in high-mobility graphene, Nat. Photon. **10**, 244-247 (2016).

[26] A. J. Frenzel, C. H. Lui, Y. C. Shin, J. Kong, and N. Gedik, Semiconducting-to-Metallic Photoconductivity Crossover and Temperature-Dependent Drude Weight in Graphene, Phys. Rev. Lett. **113**, 056602 (2014).

[27] C. H. Lui, K. F. Mak, J. Shan, and T. F. Heinz, Ultrafast Photoluminescence from Graphene, Phys. Rev. Lett. **105**, 127404 (2010).

[28] K. Oum, T. Lenzer, M. Scholz, D. Y. Jung, O. Sul, B. J. Cho, J. Lange, and A. Müller, J. Phys. Chem. C **118**, 12, 6454–6461 (2014).

[29] S. Das Sarma and Q. Li, Intrinsic plasmons in two-dimensional Dirac materials, Phys. Rev. B **87**, 235418 (2013).